Electronic Supplementary Material (ESI) for Nanoscale.

Effect of Nanoparticle Size on the Mechanical Properties of Nanoparticle Assemblies

Supplementary Information

Lu An,[a] Di Zhang,[b] Lin Zhang,[a] Gang Feng*[a]

[a]*Department of Mechanical Engineering, Villanova University, Villanova, PA 19085, USA*

[b]*Department of Mechanical Engineering, Valparaiso University, Valparaiso, IN 46383, USA*

TEM characterization

A transmission electron microscope (TEM) copper grid with a carbon film was dipped in each of the silica nanoparticle suspensions. Then each TEM grid was put in a petri dish until it was completely dried at the room temperature. TEM analyses of silica nanoparticles have been performed at 100 kV operating voltage on a Hitachi H-7600 TEM.

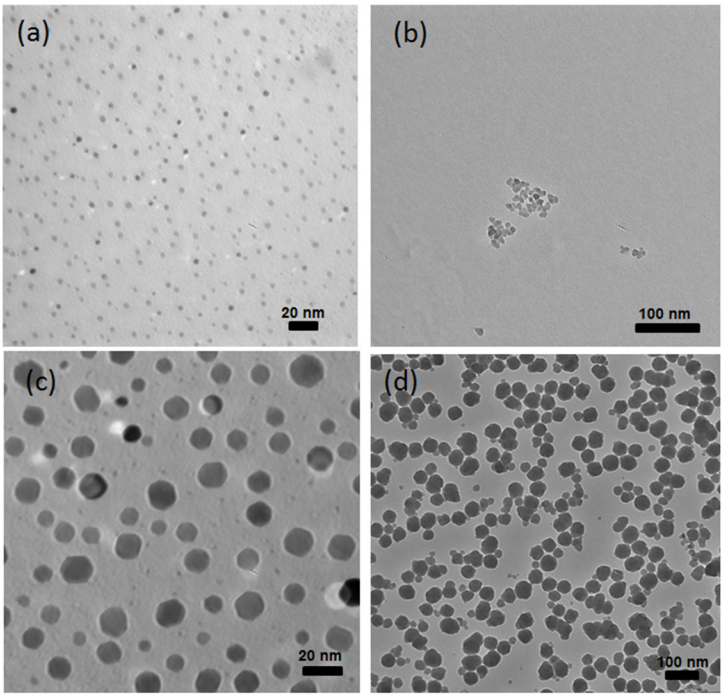

Figure S1. TEM images of (a) 4 nm, (b) 10 nm, (c) 14 nm, and (d) 59 nm SiO_2 nanoparticles purchased from Alfa Aesar™.

Porosity determination

The refractive indices of silica NPAs assembled on glass substrates were measured by using a J.A. Woollam Co. M-2000D spectroscopic ellipsometer, and the data analysis was done using the CompleteEASE™ 6.33 software package. An uncoated glass slide with a scotch tape on the backside was first scanned in the ellipsometer. Measurements were performed from 400 nm to 998.7 nm at an angle of incidence of 65°.

Using the same convective self-assembly method, 4 nm, 10 nm and 20 nm silica nanoparticle suspensions were used to fabricate thinner (100~400 nm-thick) films to satisfy the film-thickness requirement of ellipsometry. All these samples were kept in a vacuum desiccator for 2 days. The relative humidities (RH) inside the desiccator and around the ellipsometry stage were about the same at ~26%. For the silica NPAs assembled on glass substrate, we use the Cauchy model to fit the data. For the Cauchy model, the real part of the refractive index (n_{eff}) can be described by

$$n_{eff}(\lambda) = A_n + \frac{B_n}{\lambda^2} + \frac{C_n}{\lambda^4}, \qquad \text{(S1)}$$

where, A_n, B_n, C_n are fitting parameters, and λ is the light wavelength.

For each sample, seven different locations were measured by the ellipsometer. The refractive indices were determined at λ= 632.8 nm. Figure S2 shows the typical fitting curves for the 4 nm, 10 nm, and 20 nm silica NPAs, indicating that the experimental data can be fitted well using the Cauchy model.

Figures S3a shows n_{eff} and film thickness vs. d. Thus, each NPA coating's reflective index is basically the convolution of the reflective indices of all media in the coating. If the NPA contains only nanoparticles without any water, the NPA's effective refractive index n_{eff} can be estimated by the Drude model,[1-5]

$$n_{eff}^2 = n_{NP}^2(1-p) + n_{air}^2 p \ , \qquad \text{(S2)}$$

where n_{NP}=1.457 is for SiO_2 nanoparticles, n_{air}=1.00 is for air, and p is the porosity (i.e., the non-solid volume fraction). Thus, p can be estimated by Eq. S2 based on the measured n_{eff}. However, as discussed in the main text, we expect a significant amount of water in the NPAs. In the case that water also co-exists in the NPA, the NPA's n_{eff} can be estimated by the modified Drude model (Eq. S3) for the three-phase system.[1-5]

$$n_{eff}^2 = n_{NP}^2(1-f_a-f_w) + n_{air}^2 f_a + n_w^2 f_w \ , \qquad \text{(S3a)}$$

$$\text{Or, } f_a = \frac{n_{NP}^2(1-f_w) - n_{eff}^2 + n_w^2 f_w}{n_{NP}^2 - n_{air}^2} \ . \qquad \text{(S3b)}$$

where n_w=1.33 for water, f_a is the air volume fraction, and f_w is the water volume fraction. Thus, by its definition, the porosity p is the non-solid volume fraction, i.e., $p=f_a+f_w$. Provided f_w is known, Eq. S3b can be used to calculate f_a and hence p ($=f_a+f_w$). Here, f_w depends on the relative humidity (RH). As a first order approximation, f_w is assumed to be independent of d.[5] During our nanoindentation and ellipsometry measurements, the ambient RH was ~26%, which corresponds to f_w≈5.5%[5] (for a 260 nm NPA). This value of f_w≈5.5% is assumed to be approximately applied to the 4 nm, 10 nm, and 20 nm silica NPAs.

The porosity p results calculated based on Eqs. S3a-S3b are presented in Table 1 (in the main text) and Fig. S3b. Figure S3c shows the hardnesses and moduli of all NPAs including the 4 nm NPA (as highlighted).

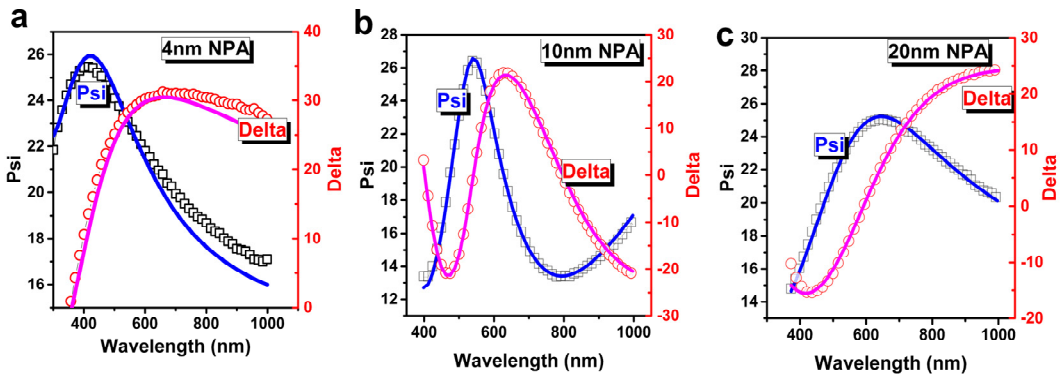

Figure S2. The experimental data (Psi and Delta, open symbols) and the fitting curves (lines) for (a) 4 nm, (b) 10 nm, and (c) 20 nm silica NPAs using the Cauchy model (Eq. S1).

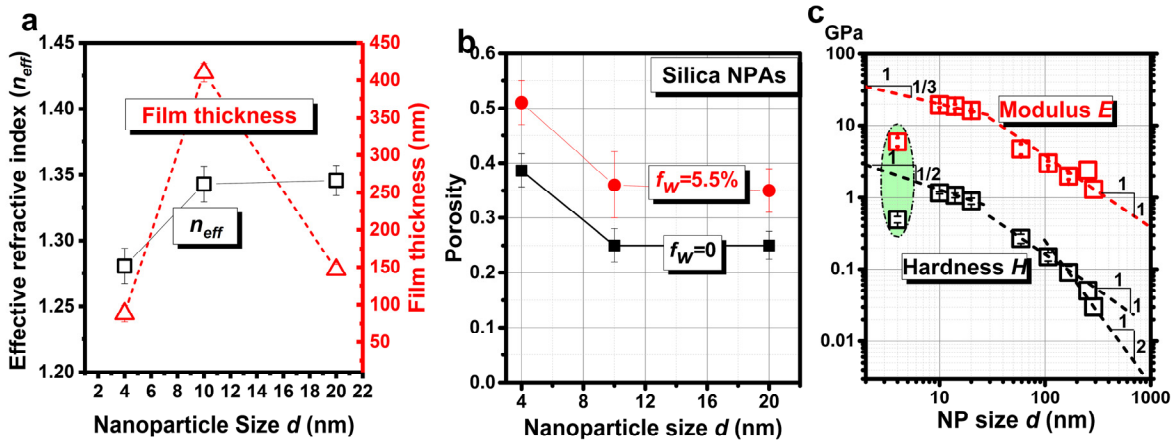

Figure S3. (a) Effective refractive index n_{eff} and thickness of silica NPAs based on the fitting using the Cauchy model. (b) Porosity p vs. d, based on two assumptions: f_w=0 and f_w=5.5%. Here, the porosity values based on f_w=5.5% are used in the paper. (c) H and E of NPAs vs. d.

Large pop-ins for NPAs

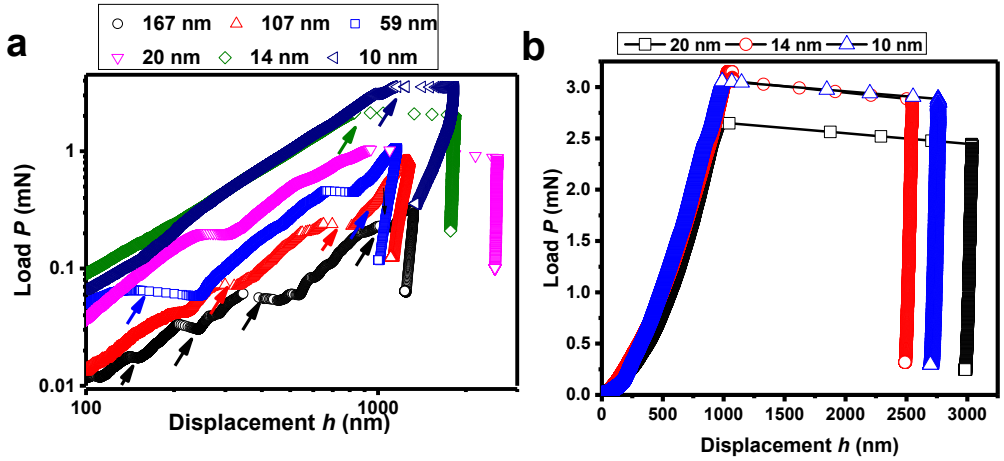

Figure S4. (a) Pop-ins for different NPAs. (b) Large pop-ins during holding at the peak load due to large cracking/delamination.

Shear bands

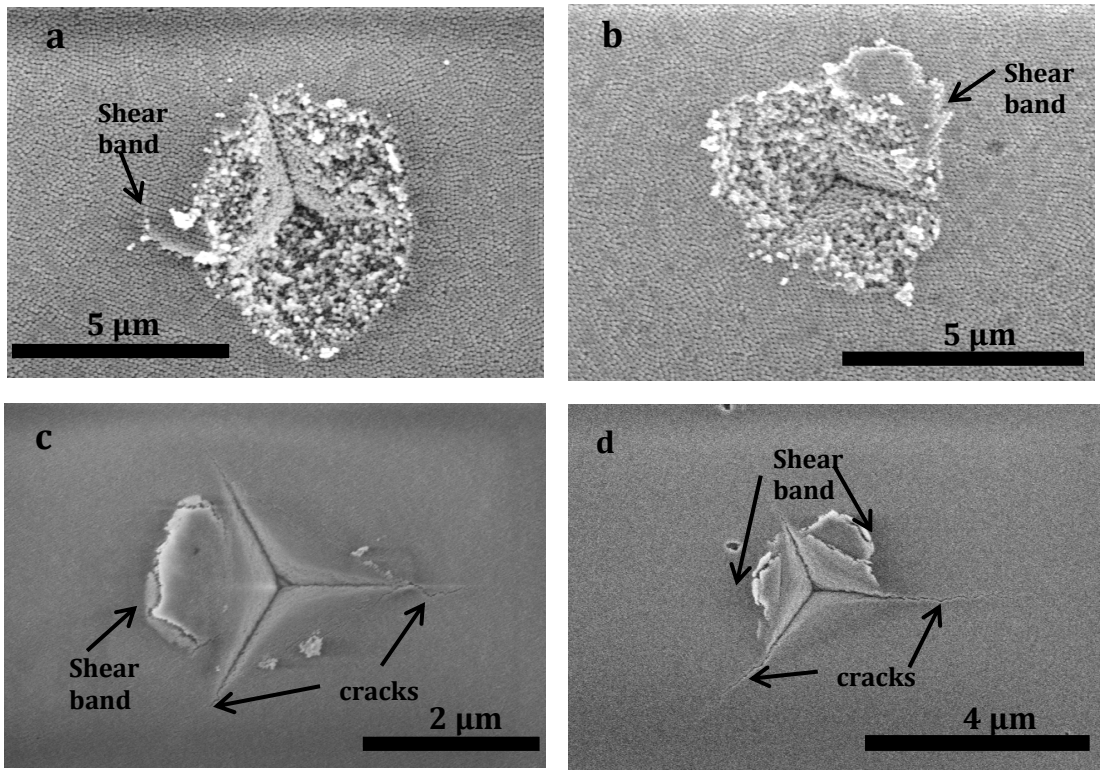

Figure S5. Indentation-induced shear bands and cracks of (a) 107 nm, (b) 59 nm (c) 20 nm (d) 10 nm SiO_2 NPAs.

Indentation-induced long cracks and/or delaminations

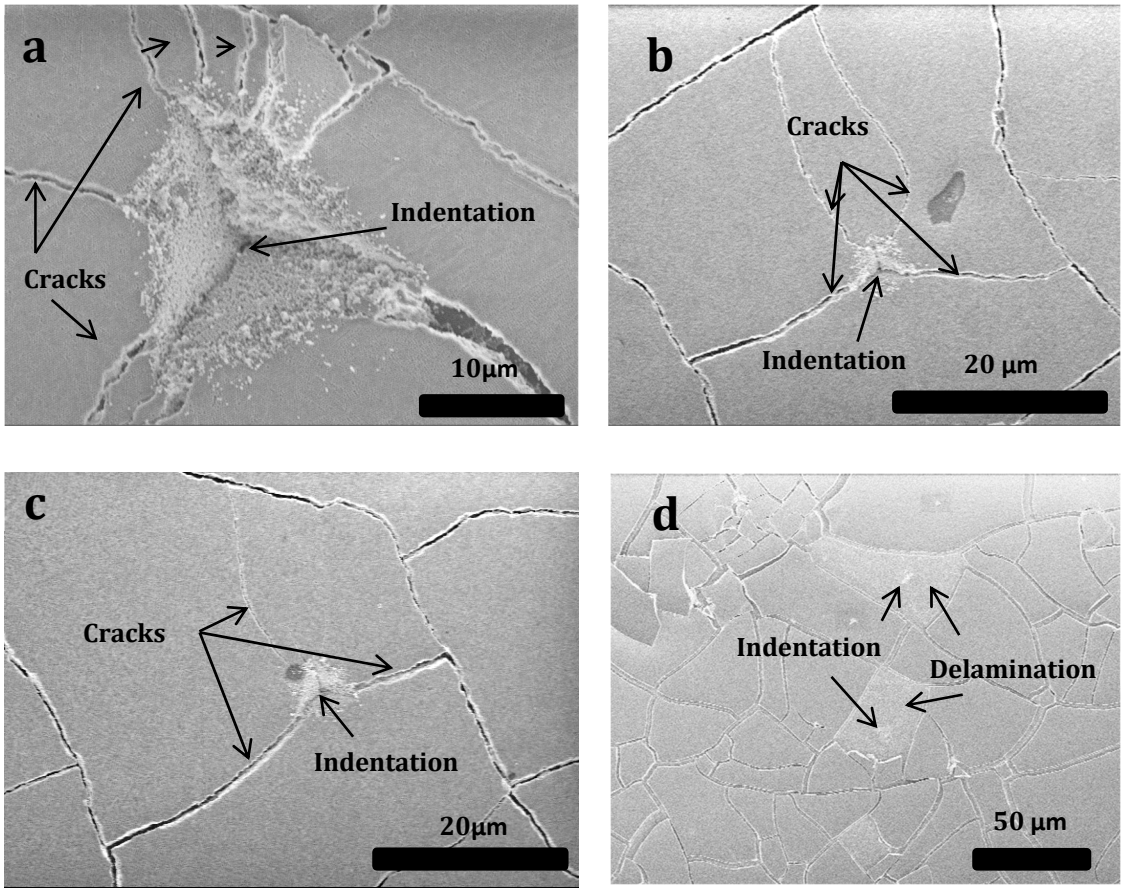

Figure S6. Indentation-induced long cracks or delaminations of (a) 167 nm, (b) 107 nm, (c) 59 nm, (d) 10 nm SiO_2 NPAs.

FTIR measurement

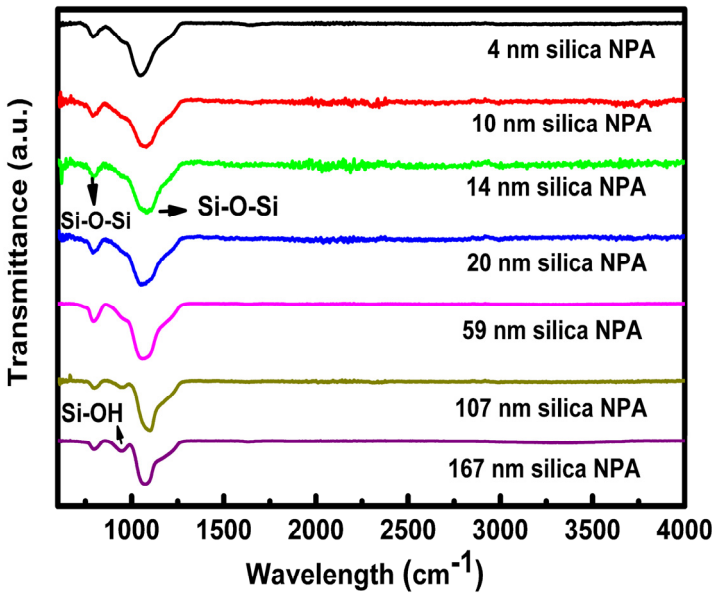

Figure S7. Fourier transform infrared (FTIR) spectra of different silica NPAs.

Fourier transform infrared (FTIR) spectra was used to investigate any possible chemical functional groups which might contribute to the inter-nanoparticle interaction besides the van der Waals and capillary interactions. Figure S7 shows three significant peaks for each sample.

The strongest peak is at ~1100 cm^{-1} with an accompanying asymmetric broad shoulder extended until ~1250 cm^{-1}. This is due to the asymmetric stretching vibration of Si-O-Si bond in the silica nanoparticles (NPs).[6-8] A smaller peak at ~800 cm^{-1} is associated with the bending mode of Si-O-Si bond.[6-8] A weak peak at ~950 cm^{-1} is due to Si-OH bond at the silica NP surface.[9]

The FTIR analysis shows only Si-O-Si and Si-OH bonds intrinsic to SiO_2 as expected for pure SiO_2 NPs. There are no any observable other functionalized head groups (e.g., -NH_2 and -COOH).

Pop-ins of all samples

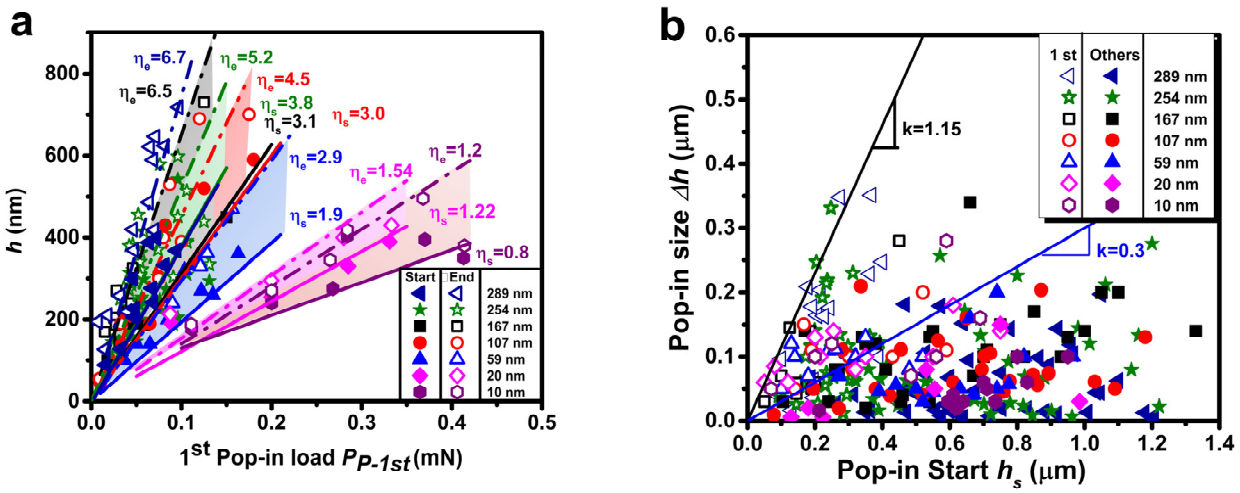

Figure S8. (a) The pop-in-start displacement h_s and pop-in-end displacement h_e of the 1st pop-in versus the 1st pop-in load P_{P1st} for 289, 254, 167, 107, 59, 20 and 10 nm SiO_2 NPAs. Here, the slopes η_s (=dh_s/dP_{P1st}) and η_e (=dh_e/dP_{P1st}) are also labeled for each sample. (b) Pop-in size Δh (=dh_e-dh_s) versus h_s for 289, 254, 167, 59, 20 and 10 nm SiO_2 NPAs.

The consistency of *P-h* curves for NPAs

More than ten nanoindentations have been performed on domain centers in each NPA sample. The *P-h* curves for each NPAs show a reasonably good consistency, as shown in Figure S9. Here we show three curves for each sample.

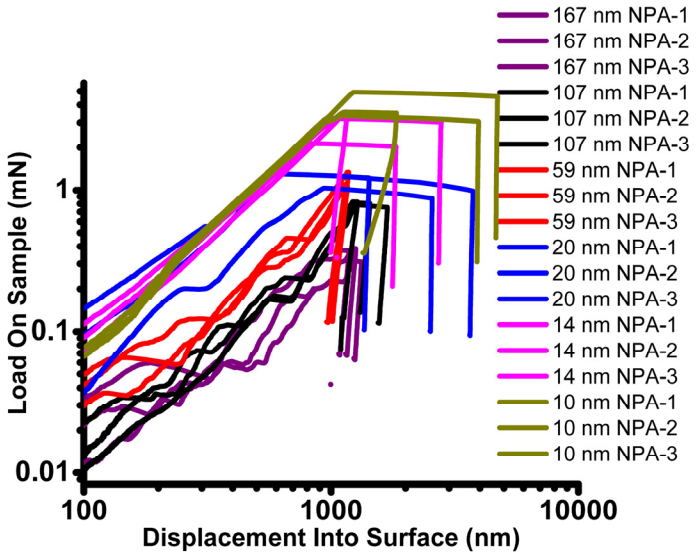

Figure S9. Load vs. displacement curves. Here, for each NPA, three data are shown.

The Oliver-Pharr method[10]

The Oliver-Pharr method is developed in 1992. It has become the most common method for analyzing the nanoindentation of thick flat homogenous materials.[10] Based on the measured load P, depth h, and elastic stiffness S obtained by the continuous stiffness measurement (CSM) technique, the contact depth h_c can be obtained as,

$$h_c = h - 0.75\frac{P}{S}. \tag{S4}$$

The contact area function relates h_c to the contact area A_c. For our cube-corner indenter, the area function is

$$A_c = 2.45182h_c^{\,2} + 905.833h_c - 2980.28h_c^{1/2} - 8184.92h_c^{1/4} + 2110.62h_c^{1/8} + 15834.3h_c^{1/16}. \tag{S5}$$

Then, the hardness H can be calculated by

$$H = \frac{P}{A_c}. \tag{S6}$$

The reduced modulus E_r can be calculated by

$$E_r = \frac{\sqrt{\pi}S}{2\sqrt{A_c}}, \tag{S7a}$$

where E_r can be correlated with the sample's Young's modulus E by

$$\frac{1}{E_r} = \frac{1-\nu^2}{E} + \frac{1-\nu_i^2}{E_i}, \tag{S7b}$$

$$\text{or, } E = \left(1-\nu^2\right)\left(\frac{1}{E_r} - \frac{1-\nu_i^2}{E_i}\right)^{-1}. \tag{S7c}$$

Here, E_i is the indenter's modulus (E_i=1141GPa for the diamond tip used). ν (=0.2 as assumed for our NPAs) and ν_i (=0.07 for the diamond tip used) are the Poisson's ratios of the sample and indenter, respectively. Thus, the sample's modulus E can be calculated by Eq. S7c.

Thus, in summary, based on the continuously measured P, S, and h, H and E can be determined continuously.

The Hay method[11]

It is fundamentally and practically important to determine the modulus of a thin film in a thin-film-on-thick-substrate system. Here, the thickness of the thin film is t. Since the system is not homogenous, if h is comparable to t, the apparent modulus value E_a calculated using the Oliver-Pharr method (Eq. S7) would have significant convolution from the substrate. This is called the substrate effect, and E_a could significantly deviate from the film modulus E_f.

Hay and Crawford developed a method in 2011[11] to correct for the substrate effect, so that E_f can be more accurately calculated for E_a. The paper of Hay and Crawford[11] is referred for the detailed discussion. Here, we briefly discuss how the Hay method can be implemented.

The sample is a thin film with a known thickness t on a thick substrate. The substrate's Young's modulus is E_s, which can be measured by directly indenting the substrate and analyzed by the Oliver-Pharr method. The Poisson's ratios of the film and substrate are assumed to be known with the values of ν_f and ν_s, respectively. Thus, the substrate's shear modulus μ_s is known and equal to $E_s/(2(1+\nu_s))$.[11]

For any indentation depth h, the contact area A_c can be calculated using Eqs. S4-S5. Based on Eq. S7c, the measured apparent shear modulus μ_a can be correlated to the measured elastic stiffness S by

$$\mu_a = \frac{1-\nu_a}{2}\left(\left(\frac{S}{2a}\right)^{-1} - \frac{1-\nu_i^2}{E_i}\right)^{-1}, \text{ where } a = \sqrt{\frac{A_c}{\pi}}. \tag{S8a}$$

where E_i and ν_i are the same as in Eq. S7c. Here, a is the contact radius. ν_a is the apparent Poisson's ratio of the system at the contact radius a and can be expressed by

$$\nu_a = 1 - \frac{\left(1-\nu_s\right)\left(1-\nu_f\right)}{1-\left(1-I_1\right)\nu_f - I_1\nu_s}, \text{ where } I_1 = \frac{2}{\pi}\arctan\left(\frac{t}{a}\right) + \frac{t}{\pi a}\ln\left(\frac{1+\left(t/a\right)^2}{\left(t/a\right)^2}\right), \tag{S9}$$

where ν_s =0.2 for the glass substrate and ν_f =0.2 for the NPAs, respectively.

Then, the film's shear modulus can be estimated by

$$\mu_f = \frac{-B+\sqrt{B^2+0.2504I_0^2\mu_a\mu_s}}{0.1252I_0}, \text{ where } B = \mu_s - \left(0.0626{I_0}^2 - I_0 + 1\right)\mu_a . \quad \text{(S10a)}$$

Here, I_0 in Eq. S10a is a weighting function based on the film thickness t and the contact radius a as

$$I_0 = \frac{2}{\pi}\arctan\left(\frac{t}{a}\right) + \frac{t}{2\pi a\left(1-\nu_a\right)}\left(\left(1-2\nu_a\right)\ln\left(\frac{1+\left(t/a\right)^2}{\left(t/a\right)^2}\right) - \frac{1}{1+\left(t/a\right)^2}\right). \quad \text{(S10b)}$$

Finally, the thin film's Young's modulus E_f at the contact radius a (and the corresponding h) can be calculated by

$$E_f = 2\mu_f\left(1+\nu_f\right). \quad \text{(S11)}$$

The comparison of moduli calculated using the Hay and the Oliver-Pharr methods

For each NPA, 10 CSM indentations were performed, and the CSM modulus results were statistically analyzed as plotted in Fig. 2c in the main text. Figure S10 plots the Oliver-Pharr moduli (solid symbols), i.e., the apparent moduli E_a, as well as the results (hollow symbols) corrected using the Hay method. For clarity, the error bars are removed. Figure S10 indicates that, for each NPA sample, the correction due to the Hay method is very small (<5%). This is due to that, compared to the film thicknesses t (>15μm), $h < t/15$, i.e., the substrate effect is expected to be small.

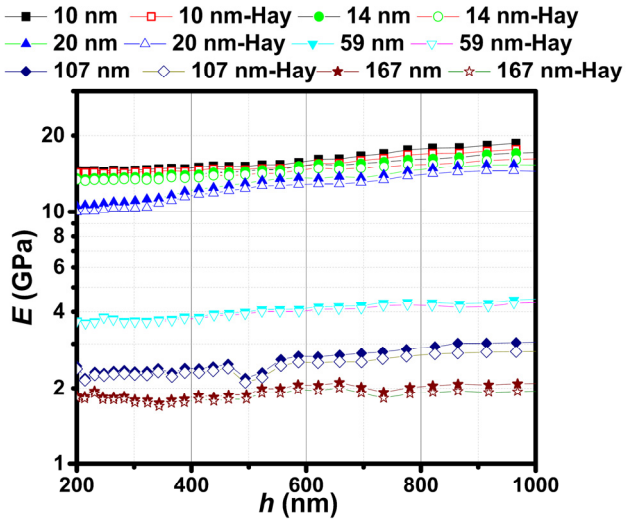

Figure S10. The comparison of moduli calculated using the Oliver-Pharr and Hay method. Here, the legend '*d* nm' indicates the modulus of the *d*-nm NPA calculated based on the Oliver-Pharr method. The legend '*d* nm-Hay' indicates the modulus of the *d*-nm NPA calculated based on the Hay method.

References

1. A. Chiappini, C. Armellini, A. Chiasera, M. Ferrari, Y. Jestin, M. Mattarelli, M. Montagna, E. Moser, G. N. Conti, S. Pelli, G. C. Righini, M. C. Gonclves and R. M. Almeida, *Journal of Non-Crystalline Solids*, 2007, **353**, 674-678.
2. M. M. Braun and L. Pilon, *Thin Solid Films*, 2006, **496**, 505-514.
3. N. J. Hutchinson, T. Coquil, A. Navid and L. Pilon, *Thin Solid Films*, 2010, **518**, 2141-2146.
4. M. Kar, B. S. Verma, A. Basu and R. Bhattacharyya, *Applied Optics*, 2001, **40**, 6301-6306.
5. F. Gallego-Gomez, A. Blanco and C. Lopez, *Advanced Materials*, 2015, **27**, 2686-2714.
6. A. Hozumi and O. Takai, *Thin Solid Films*, 1997, **303**, 222-225.
7. K. Teshima, H. Sugimura, Y. Inoue and O. Takai, *Langmuir*, 2003, **19**, 8331-8334.
8. Y. Zhao, M. Li, Q. H. Lu and Z. Y. Shi, *Langmuir*, 2008, **24**, 12651-12657.
9. C. Pereira, C. Alves, A. Monteiro, C. Magen, A. M. Pereira, A. Ibarra, M. R. Ibarra, P. B. Tavares, J. P. Araujo, G. Blanco, J. M. Pintado, A. P. Carvalho, J. Pires, M. F. R. Pereira and C. Freire, *Acs Applied Materials & Interfaces*, 2011, **3**, 2289-2299.
10. W. C. Oliver and G. M. Pharr, *Journal of Materials Research*, 2011, **7**, 1564-1583.
11. J. Hay and B. Crawford, *Journal of Materials Research*, 2011, **26**, 727-738.